**Title**
The phase space of the cubic Schrodinger equation: a numerical study



**Author**
Burlakov, Yuri

**Publication Date**
1998-05-01

LBNL-41871
Preprint


ERNEST ORLANDO LAWRENCE
BERKELEY NATIONAL LABORATORY

# The Phase Space of the Cubic Schrödinger Equation: A Numerical Study

Yuri O. Burlakov

**Computing Sciences Directorate**
**Mathematics Department**

May 1998

To be submitted
for Publication

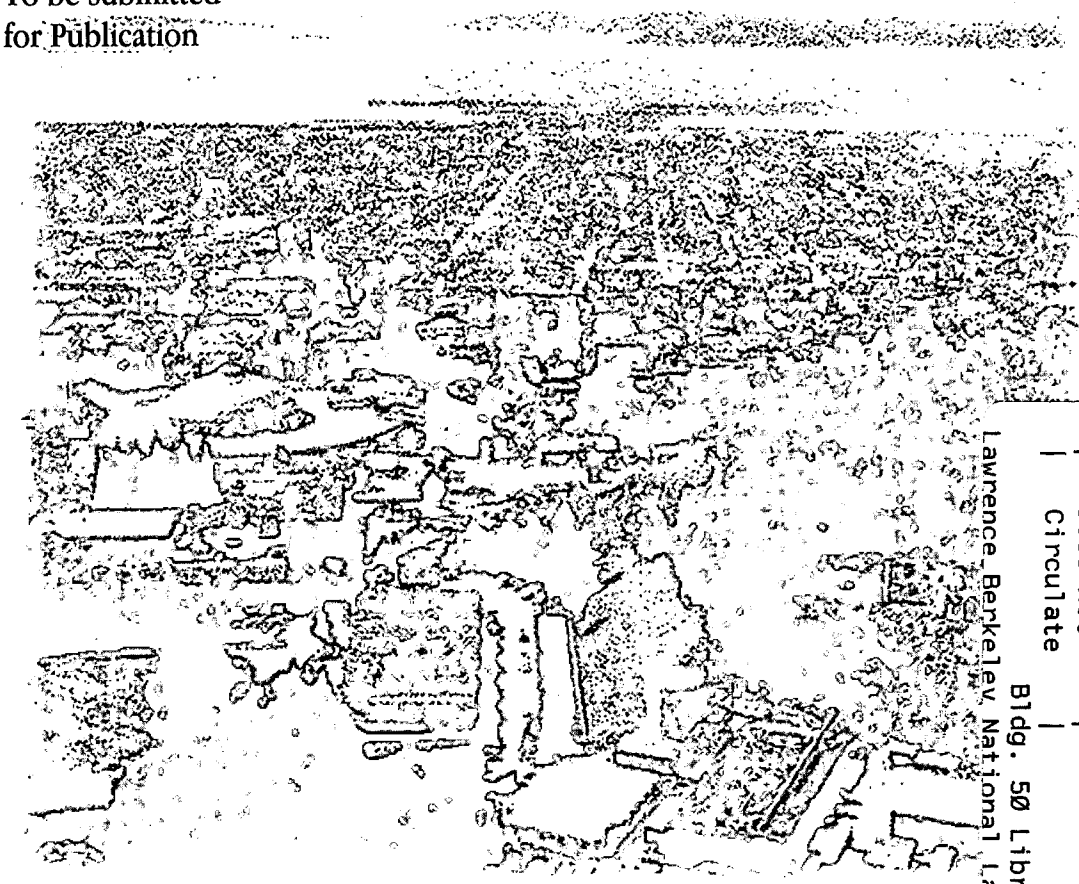

## DISCLAIMER

LBNL-41871

# THE PHASE SPACE OF THE CUBIC SCHRÖDINGER EQUATION: A NUMERICAL STUDY*

**Yuri O. Burlakov**
Lawrence Berkeley National Laboratory
and
Department of Mathematics
University of California
Berkeley, CA 94720, USA

May 1998

*This work was supported in part by the Office of Energy Research, Office of Computational and Technology Research, Mathematical, Information, and Computational Sciences Division, Applied Mathematical Sciences Subprogram, of the U.S. Department of Energy, under Contract No. DE-AC03-76SF00098, and by the National Science Foundation under Grants DMS94-14631 and DMS89-19074.

# The Phase Space of the Cubic Schrödinger equation: A Numerical Study. *

**Yuri Burlakov**
Department of Mathematics and Lawrence Berkeley National Laboratory,
University of California, Berkeley, CA 94720

**Abstract**

We study numerically a canonical ensemble of solutions of the focusing cubic Schrödinger equation. We investigate a bifurcation and a conjectured phase transition in this canonical ensemble, which were first described by Lebowitz, Rose, and Speer [11].

We show that the bifurcation and the possible phase transition are associated with the splitting of the phase space into separate components. This splitting can be observed in a discretization with as few as 2 points. We also find that in a certain continuum limit at infinite temperature there is a behavior that may be associated with a phase transition.

The cubic Schrödinger equation is equivalent to the self-induction approximation for vortices; we exhibit the changes in the shape of vortex filaments that correspond to the changes in the canonical ensemble associated with the cubic Schrödinger equation.

## 1 Introduction

The nonlinear Schrödinger equation plays a major role in describing various physical phenomena in continuum mechanics, plasma physics, nonlinear optics, and vortex dynamics in classical and superfluid mechanics. In a paper of 1988 [11] on statistical mechanics of the nonlinear Schrödinger equation, it was observed that a Gibbs canonical ensemble associated with the nonlinear Schrödinger equation exhibits behavior reminiscent of a phase transition in classical statistical mechanics. The existence of a phase transition in the canonical ensemble of the nonlinear Schrödinger equation would be very interesting and would have important implications for the role of this equation in modeling physical phenomena; it would also have an important bearing on the theory of weak solutions of nonlinear wave equations [12], [13], [14].

The cubic Schrödinger equation is equivalent to the self-induction approximation for vortices, which is a widely used equation of motion for a thin vortex filament in classical and

*This work was supported in part by the Applied Mathematical Sciences Subprogram of the Office of Energy Research, U.S. Department of Energy, under contract DE-AC03-76-SF00098, and in part by the National Science Foundation under grants DMS94-14631 and DMS89-19074.

superfluid mechanics [8]. The existence of a phase transition in such a system would be very interesting and actually very surprising for the following reasons: in classical fluid mechanics it is believed that the turbulent regime is dominated by strong vortex stretching [4], while the vortex system described by the cubic Schrödinger equation does not allow for stretching. In superfluid mechanics the self-induction approximation and its modifications have been used to describe the motion of thin superfluid vortices [17], which exhibit a phase transition; however, more recently some authors concluded that these equations do not adequately describe superfluid turbulence [3], and the absence of a phase transition in the cubic Schrödinger equation would strengthen their argument. The self-induction approximation for vortices takes into account only very localized interactions, and the existence of a phase transition in such a simplified system would be very unexpected.

In this paper we present a numerical study of the phenomena observed in [11]; in particular, we find that these phenomena are strongly related to the splitting of the phase space into distinct components. We point out the interesting fact that the splitting can be observed in a discretization with as few as 2 points. The refinement of the discretization does not change the global picture qualitatively.

We vary two parameters in the canonical ensemble of the cubic Schrödinger equation: the first is the temperature, the second is a certain constraint on the function space. We demonstrate that at a fixed low temperature, as the constraint varies, the canonical ensemble of the cubic Schrödinger equation undergoes a bifurcation which is manifested both in the change in the shape of the typical function and in a corresponding change of the structure of the phase space.

For a fixed value of the constraint, as temperature varies, there is a change in the shape of the typical function and a corresponding change in the structure of the phase space. We investigate numerically a special continuum limit in which both the constraint and the number of discretization points increase, and conclude that there is a strong indication of a phase transition in this limit. We also discover that in terms of vortex approximations, the phase transition type behavior for the cubic Schrödinger equation results in the transition from an almost straight filament with a sharp kink for low temperatures to a filament of random shape at high temperatures.

We show that the canonical ensemble associated with the cubic Schrödinger equation, in a sense to be made precise later, is equivalent to the microcanonical ensemble. We also present numerical results that show the equivalence of the time and ensemble averages.

# 2 Formulation of the Problem

The cubic Schrödinger equation

$$\frac{1}{i}\frac{\partial \psi}{\partial t} = \frac{\partial^2 \psi}{\partial x^2} + |\psi|^2 \psi \tag{1}$$

where $\psi$ is a complex function of scalar arguments $t$, and $x$

$$\psi(t,x) = q(t,x) + \imath p(t,x), \tag{2}$$

can be rewritten in the Hamiltonian form:

$$\frac{\partial q}{\partial t} = -\frac{\partial^2 p}{\partial x^2} - p(q^2+p^2) = \frac{\delta H}{\delta p}, \qquad \frac{\partial p}{\partial t} = \frac{\partial^2 q}{\partial x^2} + q(q^2+p^2) = -\frac{\delta H}{\delta q}, \tag{3}$$

where the Hamiltonian is

$$H(p,q) = \frac{1}{2}\int_0^L [(\frac{\partial q}{\partial x})^2 + (\frac{\partial p}{\partial x})^2]dx - \frac{1}{4}\int_0^L (q^2+p^2)^2 dx, \tag{4}$$

and $\frac{\delta H}{\delta p}, \frac{\delta H}{\delta q}$ denotes functional derivatives. Lebowitz et al. ([11]) introduced an ensemble very similar to Gibbs canonical ensemble, with a measure formally written as:

$$\mathbf{P}(dp,dq) = Z^{-1}\exp[-\beta H(p,q)]dpdq, \tag{5}$$

or, writing the Hamiltonian explicitly:

$$\mathbf{P}(dp,dq) = Z^{-1}\exp[-\beta\frac{1}{2}\int_0^L ((\frac{\partial q}{\partial x})^2 + (\frac{\partial p}{\partial x})^2)dx]\exp[\beta\frac{1}{4}\int_0^L (q^2+p^2)^2 dx]dpdq, \tag{6}$$

where dpdq is a Lebesgue measure, Z is a partition function, and $\beta$ is a scalar, the 'inverse temperature'. The Hamiltonian (4) is not bounded below, so in order to make sense out of a formal object (5) Lebowitz et al. suggested to restrict the ensemble to the functions that satisfy either

$$\int_0^L (q^2+p^2)dx = N, \tag{7}$$

or

$$\int_0^L (q^2+p^2)dx \leq N, \tag{8}$$

for some constant $N$, so that the second term in (6) can be bounded by the first. They proved that this constrained measure is well defined (see [11] for details); we assume here and everywhere in this paper that p and q are periodic functions of x, and the constraint is given by (7). The choice of these constraints was motivated by the fact that the nonlinear Schrödinger equation conserves the integral (7).

# 3 Preliminary Results

We now present numerical results on the behavior of the measure (6),(7) which are directly linked to the phase transition type behavior observed in [11].

In [11] it was observed that for different ranges of temperatures and constraints the measure (6),(7) is concentrated on functions of different shapes. As an example, we present several typical functions for low and high temperature, and low and high values of constraint in Figures (1),(2),(3).

In order to distinguish between the functions the following quantity was introduced in [11]:

$$K = \frac{< \int_0^L (q^2(x)+p^2(x))^2 dx >}{< \int_0^L (q^2(x)+p^2(x))dx >^2}. \tag{9}$$

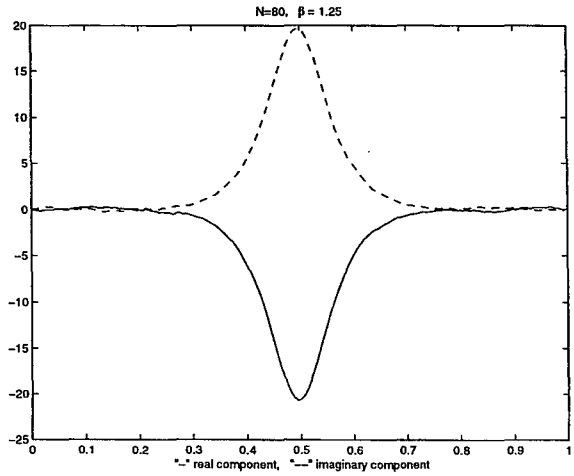


Figure 1: Typical real and imaginary components of the field for low temperature and large value of the constraint.

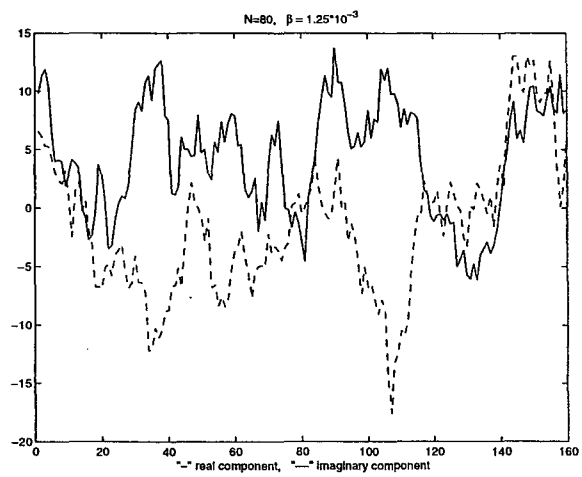


Figure 2: Typical real and imaginary components of the field for high temperature.

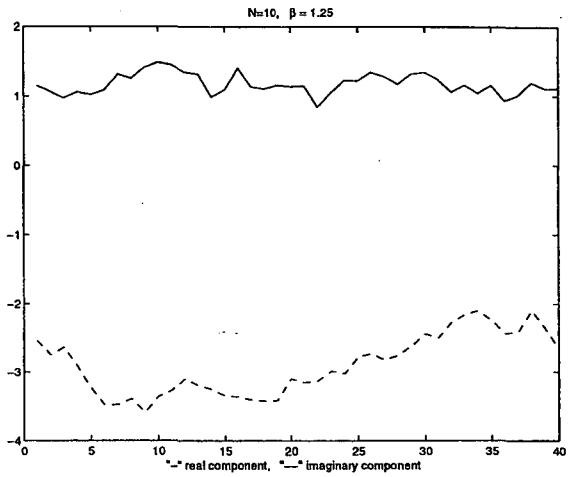


Figure 3: Typical real and imaginary components of the field for low temperature and small value of the constraint.

The denominator in (9) is used for the normalization; recall that our measure must satisfy the constraint (7), therefore (9) can be rewritten in the form

$$K = \frac{< \int_0^L (q^2(x) + p^2(x))^2 dx >}{N^2}. \tag{10}$$

In Figure (4) we plot $K$ for various $N$ and temperature.

Notice that on the left side of the picture in Figure (4) ( $10^{-2} \leq \frac{1}{\beta N} < 1$ ) the three curves are distinctly different and almost constant; in the transition region $1 \leq \frac{1}{\beta N} \leq 10$, the curves come together, and for $10 \leq \frac{1}{\beta N} \leq 10^2$ the three curves assume the same constant value.

This behavior of the kurtosis $K$ is very similar to what has been observed in certain phase transitions in statistical physics [9], and it raises the question as to whether this is indeed a phase transition or if some other phenomenon is taking place.

In order to examine this question we start by studying a simplified system, and then move to a more general one.

First we introduce a discretization of the Hamiltonian (4) and of the constraint (7). Discretize the interval [0,L] by n discretization points; let $u_i$ and $v_i$ be the discretization of the real and imaginary part of the solution of the cubic Schrödinger equation; then the discrete version of the Hamiltonian (4) is

$$H = \frac{1}{2}\sum_{i=1}^{n}((\frac{u_{i+1}-u_i}{h})^2 + (\frac{v_{i+1}-v_i}{h})^2)h - \frac{1}{4}\sum_{i=1}^{n}(u_i^2+v_i^2)^2 h, \tag{11}$$

where h $= \frac{L}{n}$ is the discretization step. This particular discretization of the Hamiltonian leads to the following discretization of the measure (6)

$$\mathbf{P}(du,dv) = Z_n^{-1}\exp[-\beta[\frac{1}{2}\sum_{i=1}^{n}((\frac{u_{i+1}-u_i}{h})^2 + (\frac{v_{i+1}-v_i}{h})^2)h - \frac{1}{4}\sum_{i=1}^{n}(u_i^2+v_i^2)^2 h]]dudv, \tag{12}$$

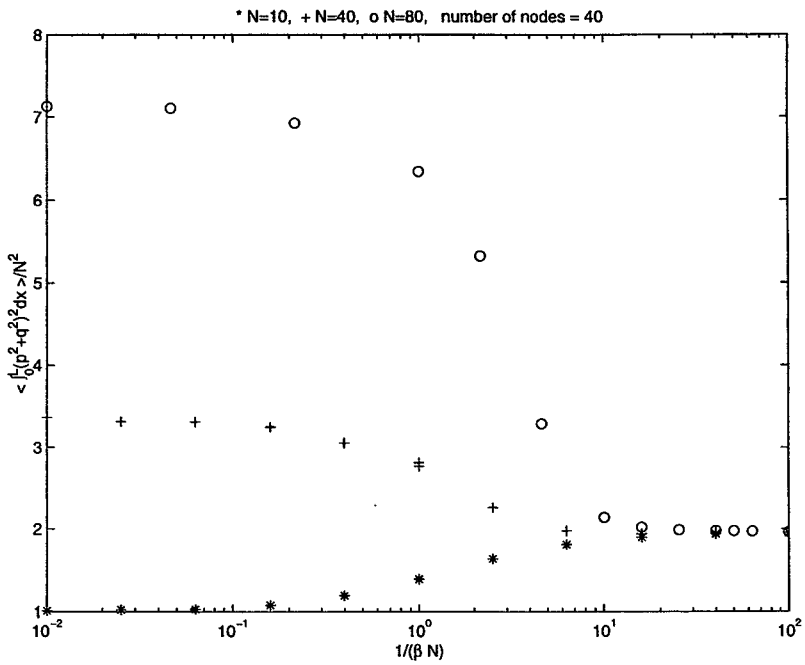


Figure 4: Values of K for N= 10, 40, 80 and varying $\beta$.

and the discretization of the constraint (7) is

$$N = \sum_{i=1}^{n} (u_i^2 + v_i^2)h. \tag{13}$$

Suppose we are given a discrete canonical measure (12),(13), and we want to compute an average with respect to this measure of some quantity using the Metropolis sampling algorithm [15], [2]. We start with some random initial configuration, which we denote by $x_1 \equiv (u(1), \ldots, u(n), v(1), \ldots, v(n))$, and then run the Metropolis sampling for some large number of steps $M$, storing each configuration as a point $x_i$, $i = 1, \ldots, M$. After $M$ steps we will get $M$ points, $(x_1, \ldots, x_M)$; this collection of $M$ points we will call a Metropolis sampling trajectory. Notice that this Metropolis sampling trajectory does not depend on a quantity computed in the Metropolis sampling algorithm; it only depends on the temperature in the ensemble and on the initial point.

The Metropolis sampling trajectory is a trajectory in 2n-dimensional space; we can define a projection of the Metropolis sampling trajectory onto a 3-dimensional subspace by picking any three components of the vectors $u$,$v$, for example $u_1, u_2, v_3$.

Now consider a time dependent Hamiltonian system with periodic boundary conditions (3); discretize this system in space by n points, and integrate it in time for some large time T, starting at some initial configuration $y_1 \equiv (u(1), \ldots, u(n), v(1), \ldots, v(n))$. For integration in time we use some numerical method, for example the one described in [10]; we define the time trajectory as a collection of points $(y_1, \ldots, y_K)$, $K\Delta t = T$, where $\Delta t$ is the time step of the numerical integration scheme. The time trajectory is a trajectory in 2n-dimensional space, and a projection of the time trajectory onto a three-dimensional subspace we will call a projected time trajectory.

# 4 The Simplest Case

To motivate the discussion later in this paper we consider a very simple discrete periodic in space system (11),(13) with just 2 discretization points, i.e. in (11), (13) we take $n = 2$.

The reason for choosing such a system is its simplicity; we can visualize this system in 3-dimensional space, because this system is almost 3-dimensional. By almost 3-dimensional we mean that given three arbitrary components of the system, for example $u_1, u_2$, and $v_1$, one can determine $v_2$ from (13) up to a sign.

In Figure (5) we present the graphs of $K$ vs. $\frac{1}{\beta N}$ for several different values of $N$.

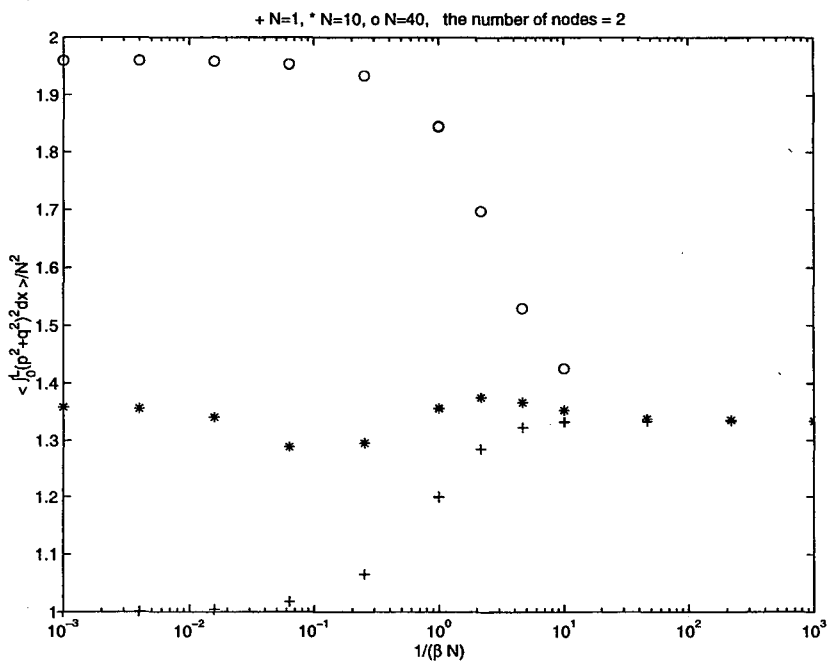


Figure 5: Values of K for N= 1, 10, 40 and varying $\beta$.

Notice that even for the simple 2 node system there is qualitative similarity between these graphs and the ones in Figure (4) for the 40 node system. This indicates that studying a simple 2 node system will provide an insight into the behavior of a more complicated one.

In Figure (5) as in Figure (4) there are clearly three distinct regimes; for $10^{-3} \leq \frac{1}{\beta N} \leq 10^{-1}$ the curves corresponding to different constraints are clearly distinct and almost constant; for $10^{-1} \leq \frac{1}{\beta N} \leq 1$ the curves come together, and for $1 \leq \frac{1}{\beta N}$ the curves are indistinguishable and constant.

We would like to find out what are the changes in Metropolis sampling trajectories corresponding to the different curves in Figure (5).

In Figure (6) we plot a Metropolis sampling trajectory for low temperature and small constraint; the parameters corresponds to the left side of the lower curve in Figure (6). We started the Metropolis sampling at many different points and each time got the same torus as in Figure (6).

Now we consider how this Metropolis sampling trajectory changes as we increase the

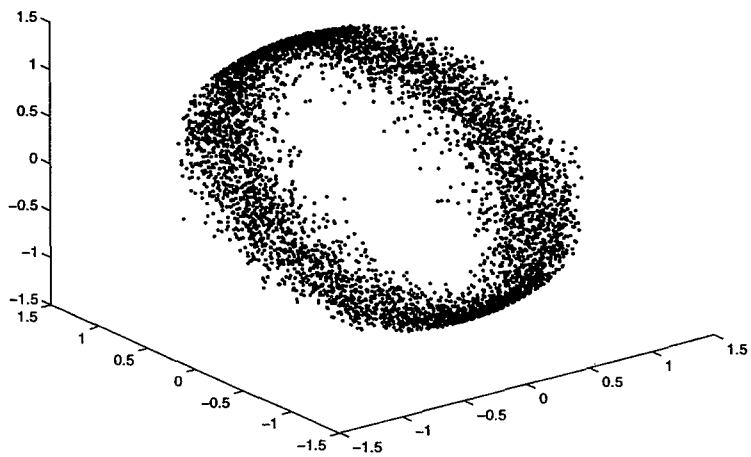


Figure 6: Metropolis sampling trajectory of the 4-dimensional system, $\beta$=4. The axes correspond to the two real components and one of the imaginary components of the system.

temperature. We pick some high value of temperature, and compute the Metropolis sampling trajectories starting at various initial configurations. What we see is that the torus-like structure of the most important configurations changes completely and starts to look like a ball.

We observe that the typical phase space Metropolis sampling pattern completely changes its shape over some range of values of temperature; there is a low temperature pattern - a torus, a high temperature pattern - a ball, and a transition region between them, in which torus is transformed into a ball. The ball pattern corresponds to the curves on the right side in Figure (5).

We would like to find what are the changes in the Metropolis sampling trajectories corresponding to the low value of $\frac{1}{\beta N}$ when the three curves in Figure (4) are distinct. To do this we fix $\frac{1}{\beta N} = 10^{-2}$ and plot Metropolis sampling trajectories in Figures (8), (9), and (10), for $N$=1, 10, and 40 respectively.

A new interesting feature has appeared in Figure (9) as we increase the value of the constraint $N$ from 1 to 10 — a single torus splits into two tori, and the two tori then move apart as $N$ increases until they become perpendicular to each other.

In order to see what happens to the two tori Metropolis sampling trajectories ($N = 40$) as we increase the temperature, we pick the first value of $\beta$ in the transition region, for example $\frac{1}{\beta N} = 1$, and the second value of $\beta$ in the region where all three curves in Figure (5) come together, for example $\frac{1}{\beta N} = 10$. The Metropolis sampling trajectories are shown in Figures (11), and (12).

One can see from these pictures that as temperature increases the two tori become 'fatter' in the transition region, and turn into a ball for high enough temperatures.

It is intuitively clear that for low temperatures the Metropolis sampling trajectories are

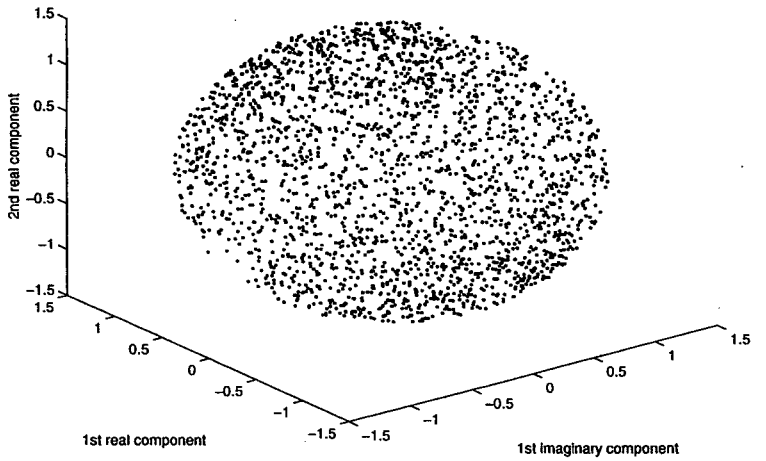


Figure 7: Metropolis sampling trajectories of the 4-dimensional system with constraint, $\beta$=0.04. The axes correspond to the two real components and one of the imaginary components of the system.

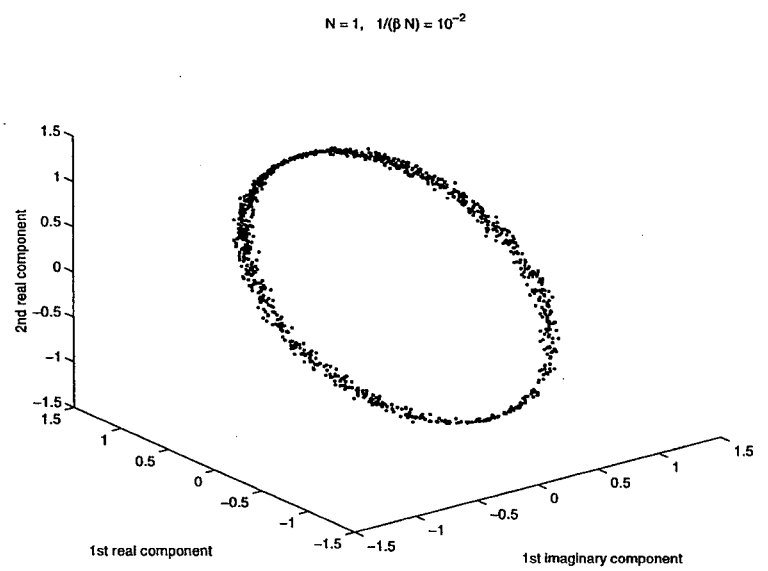


Figure 8: Metropolis sampling trajectories of the 2 node system, $N = 1$, $1/(\beta N) = 10^{-2}$.

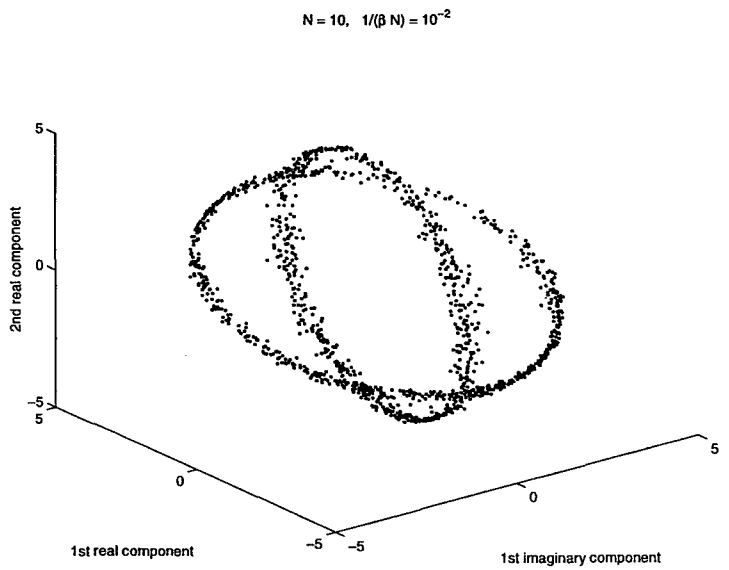


Figure 9: Metropolis sampling trajectories of the 2 node system, $N = 10$, $1/(\beta N) = 10^{-2}$.

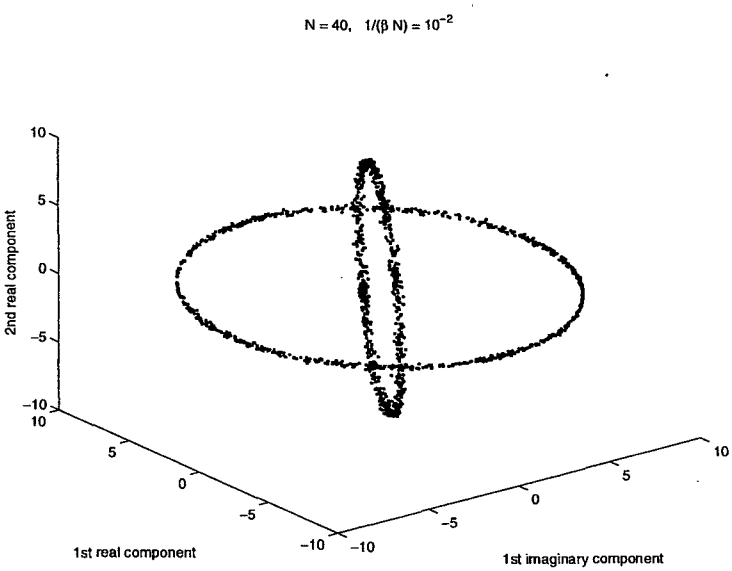


Figure 10: Metropolis sampling trajectories of the 2 node system, $N = 40$, $1/(\beta N) = 10^{-2}$.

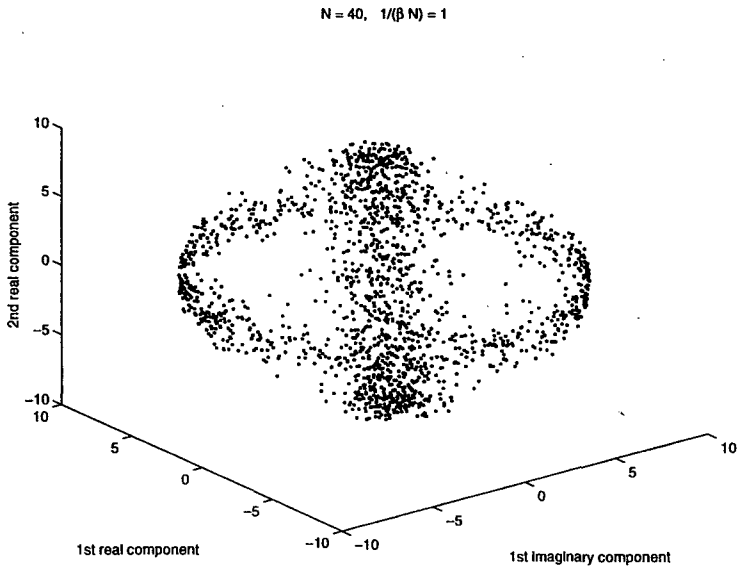


Figure 11: Metropolis sampling trajectories of the 2 node system, $N = 40$, $1/(\beta N) = 1$.

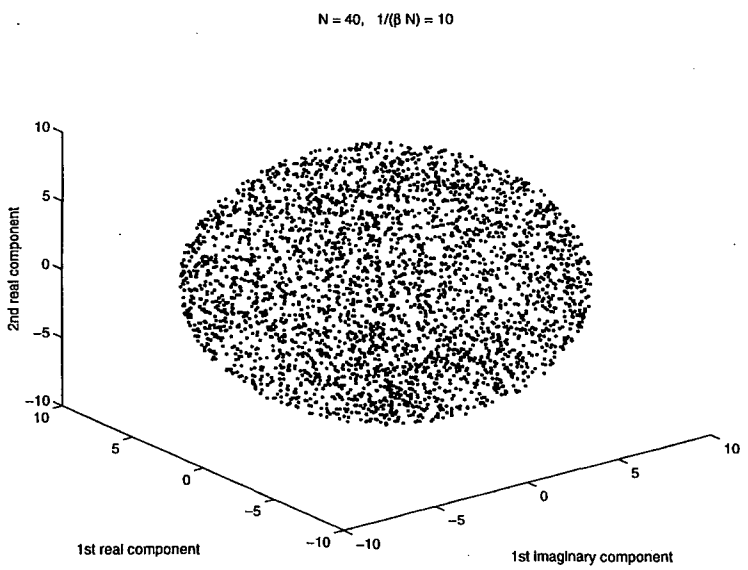


Figure 12: Metropolis sampling trajectories of the 2 node system, $N = 40$, $1/(\beta N) = 10$.

concentrated around the minimum energy time trajectories; below we present minimum energy time trajectories for $N = 10$, (Figure (13)), and for $N = 40$ (Figure (14)).

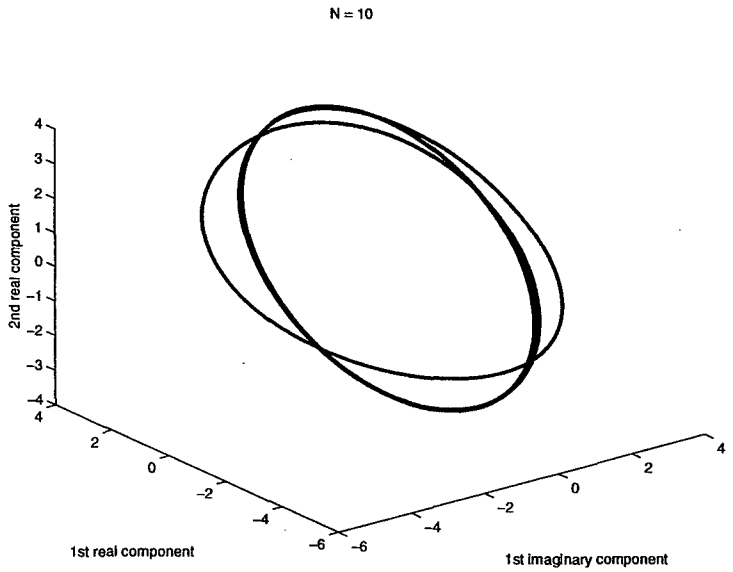


Figure 13: Splitting of the minimum energy circle in the time dependent system, $N = 10$.

Recall that there are two time trajectories coming through each point of the phase space, since the fourth degree of freedom of the system is determined from the three shown in the picture and a constraint up to a plus or a minus sign.

If we compare Figures (13), (14) and Figures (9),(10) respectively, we again see a very good agreement between Metropolis sampling and time trajectories.

# 5 The General Case

Now we consider the more general case of the statistical ensemble (12),(13), and a dynamical system (3) with the number of discretization points $n$ greater than 2. We would like to investigate the connection between changes in kurtosis (4) and Metropolis sampling trajectories; we are motivated by the simple 2 point system case of the preceding section, and would like to see whether such phenomena as tori turning into a ball persists for the large system. Since we cannot visualize the whole $n$-point system as we could before, we have to take projections onto a three-dimensional subspace.

Surprisingly, we are still able to observe very clearly the phase space changes of the Metropolis sampling trajectories at low and high temperatures, which look very much the same as in the simple 2-point case.

We present a typical picture that we observed over different combinations of any three discretization nodes. We picked at random three particular nodes and monitored their Metropolis sampling trajectories for a few different runs of Metropolis algorithm.

In Figure (15) we present the projection of the Metropolis sampling trajectory of a 10-point system for low temperature. The parameter range of this system ($N = 1$, $\beta = 4$)


Figure 14: Splitting of the minimum energy circle in the time dependent system, $N = 40$.

corresponds in Figure (4) to the left part of the lower curve ($\frac{1}{\beta N} = 0.25$). Notice that the Metropolis sampling trajectory is a single torus and looks very much the same as the torus of the 2-point system in Figure (6).

Both of these tori in Figures (15), and (6) correspond to the lower kurtosis curves in Figures (4), and (5) respectively.

In the 2-point case we observe that as we increase the temperature the torus like picture turns into a ball. Now we increase the temperature in the large system ($\frac{1}{\beta N} = 10$, see Figure 4) and plot the resulting Metropolis sampling trajectories in Figure (16).

Observe that the torus turns into a ball, just as in the 2-point system (see Figures (6),(7)). This is very surprising; even though the phase space of the larger system is very complicated, the simple phase space structure of the Metropolis sampling trajectories is preserved in the large system.

Let us consider the dynamical system (3); which we discretize with a large number of points and integrate in time at a minimum value of the Hamiltonian; the resulting trajectory is given in Figure (17).

Notice that, as before in the 2-point case, the Metropolis sampling trajectories for low temperature (Figure 15) are concentrated around the energy minimum shown in Figure (17).

Recall that in Figure (4) kurtosis changes depending on both temperature and constraint $N$. In the simple 2-node system we observed that as $N$ increases at low temperature, the torus splits into two tori (Figures 8, 9, 10 ). The sample trajectories of the large system also change from a torus to a more complicated structure, which we plot in Figure (18); nevertheless the torus like picture splits into something very similar to the two tori picture of the simple 2-point system (see Figure 10).

As temperature increases, something similar to the 2-point case takes place; at first the tori structure becomes 'fatter' (see Figure 19) and then for high temperature it turns into a ball (Figure 20).

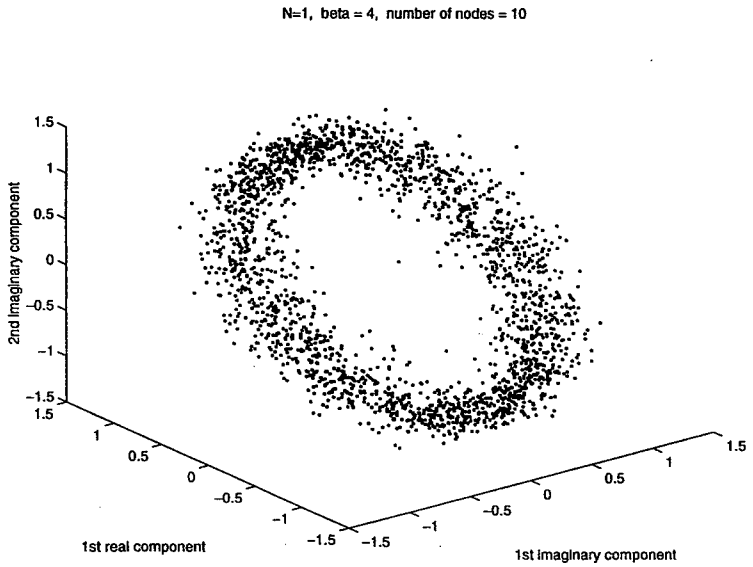


Figure 15: Metropolis sampling trajectory for the 10-point system, N=1, $\beta = 4$.

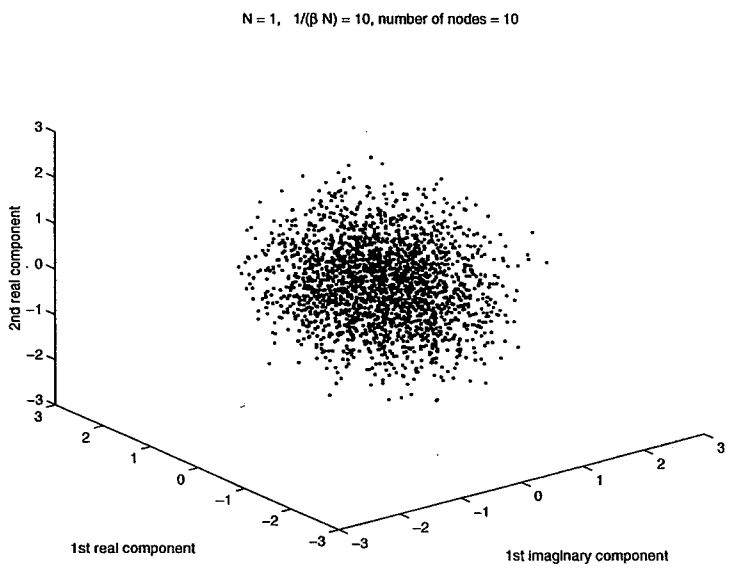


Figure 16: Metropolis sampling trajectory for the 10-point system, N=1, $\beta = 0.1$.

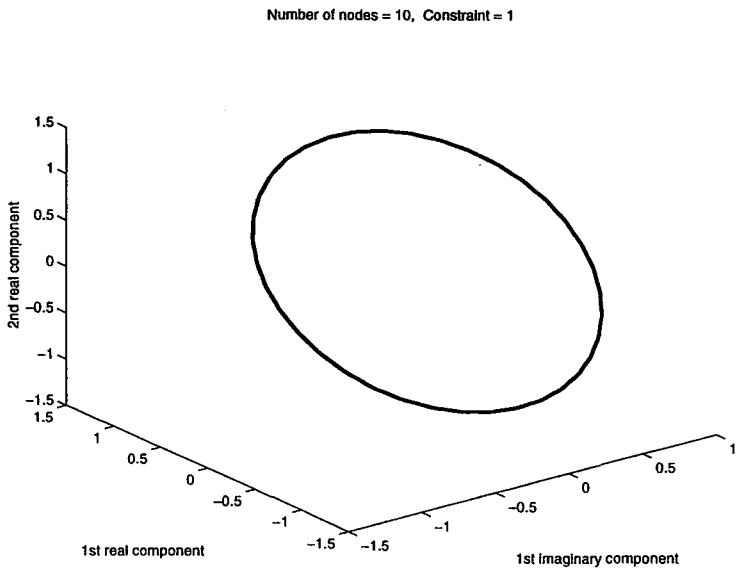


Figure 17: Projected time trajectory of the 10-point system for small energy.

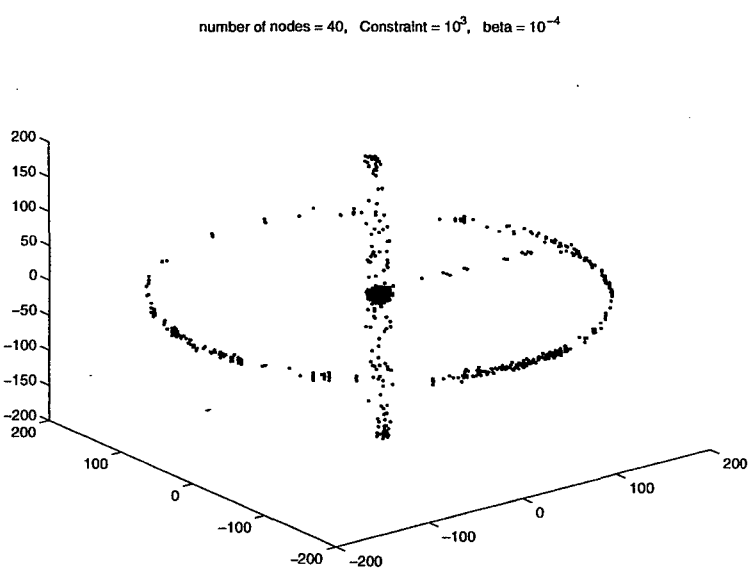


Figure 18: Metropolis sampling trajectory for the 40-point system $N = 10^3$, $\beta = 10^{-4}$.

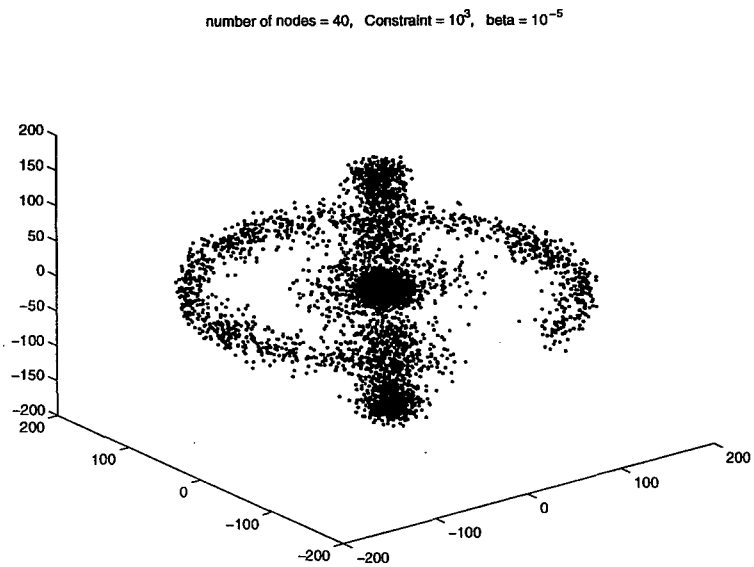


Figure 19: Metropolis sampling trajectory for the 40-point system $N = 10^3$, $\beta = 10^{-5}$

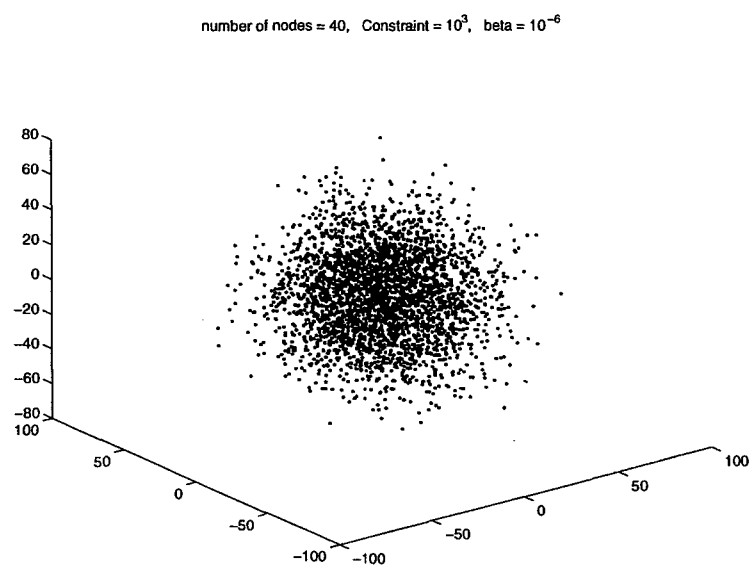


Figure 20: Metropolis sampling trajectory for the 40-point system $N = 10^3$, $\beta = 10^{-6}$

Clearly, there is a strong connection between phase space Metropolis sampling trajectories structure and differences in kurtosis (Figure 4), which appears in the small 2-node system and persists for larger systems.

It might appear that as $N$ increases for low temperature the kurtosis curves in Figure (4) will tend to a discontinuous step function. However, what really happens for a fixed number of discretization points is that for large enough value of N the curves converge to a smooth function; the results are shown in Figure (21).

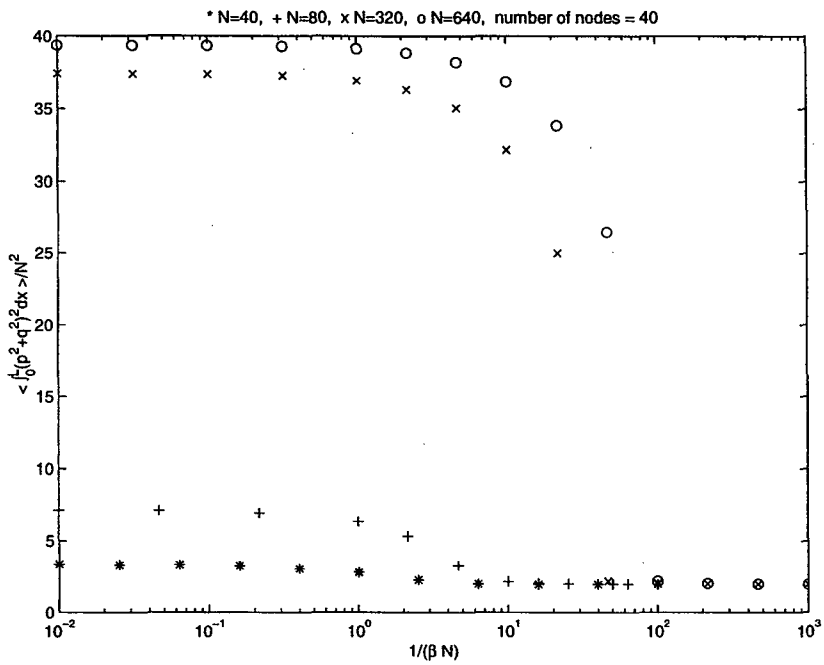


Figure 21: Values of K for various N and $\beta$

For values of $N > 640$ presented in Figure (21) the curves converge to a curve close to the one that corresponds to $N = 640$. From these pictures for the fixed number of nodes we do not observe convergence to the discontinuous step function as N increases.

Now consider the limit in which the constraint $N$ is fixed and the number of discretization points increases. In this case again we observe that the functions converge to some smooth limit function; the results are shown in Figure (22).

If we pick a larger value of $N$ and compute kurtosis for increasing numbers of discretization points, the functions again converge to some smooth limit function; the results are shown in Figure (23).

These plots suggests that for a fixed value of $N$, as the number of discretization points increases the kurtosis converges to a smooth function. However, for larger value of $N$ the kurtosis has a steeper slope in the transition region; this suggests that we need to investigate the limit as both $N$ and the number of discretization points increase.

We are going to show that as we increase the number of discretization points the kurtosis tends towards to a higher limit.

In the previous plots we either used a fixed number of discretization nodes (n=40) or a

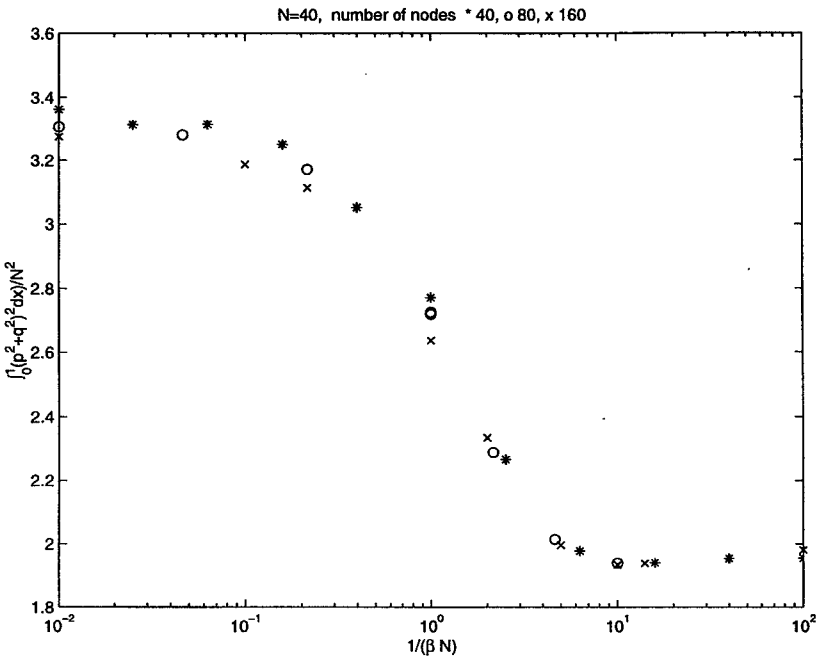


Figure 22: Values of K for N=40 and different number of discretization points.

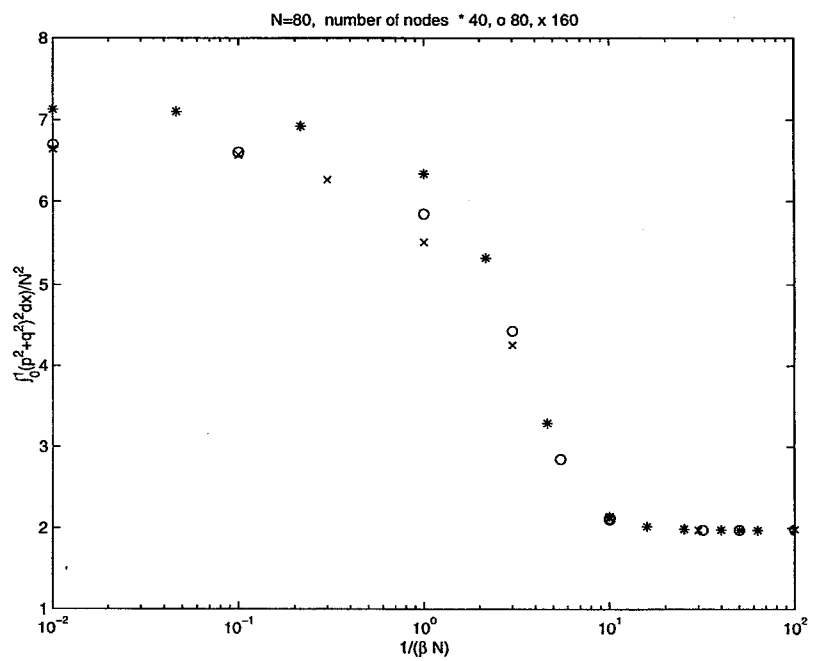


Figure 23: Values of K for N=80 and different number of discretization points.

fixed constraint ($N$=40, $N$=80). If we now increase the number of discretization points and the constraint $N$ simultaneously, we observe that in the transition region the slope of the curve corresponding to larger $N$ is steeper than for a smaller $N$. If we double the number of nodes, the derivative increases substantially (see the summary in Table (1)). This might suggest the possibility of a discontinuity in the function K in the limit as $N$ and the number of discretization points approach infinity. The estimates for the derivatives in the transition region are summarized in Table (1).

| Number of nodes | Maximum absolute value of the derivative |
|---|---|
| 40 | 2.1 |
| 80 | 14.1 |
| 160 | 22 |
| 320 | 30.5 |

Table 1: Maximum absolute value of the derivative

The plots of the curves in the transition region are given in Figure (24). Here we plot K for increasing number of nodes and increasing values of N. Notice that in Figures (21), (22), (23) we used a logarithmic scale, but we do not use it in Figure (24).

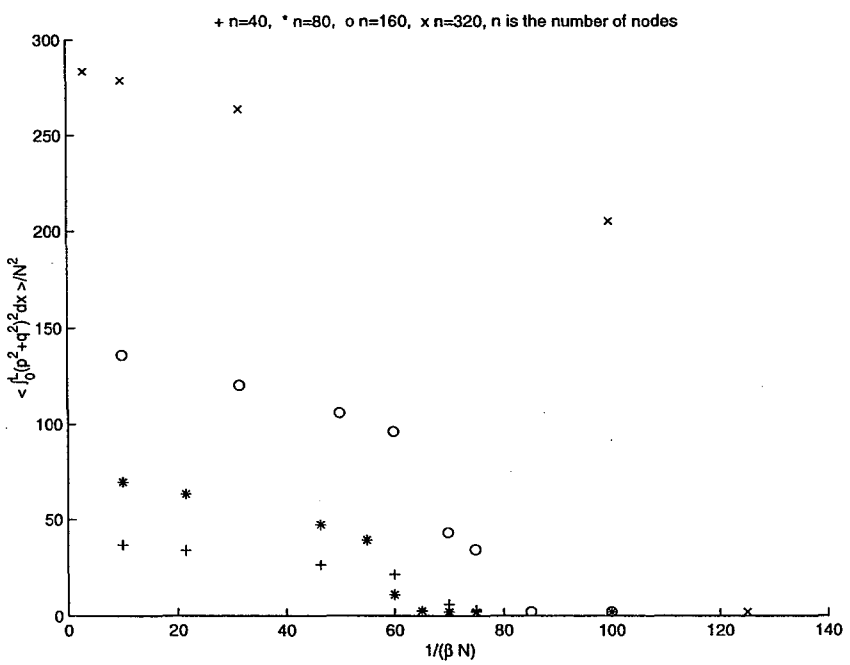


Figure 24: Values of K for increasing number of discretization points and $N$. $N = 640$ (for 40 and 80 nodes), $N = 1000$ (for 160 nodes), and $N = 2000$ (for 320 nodes)

Also observe that the horizontal axis in Figure (24) is scaled as $\frac{1}{\beta N}$, and as $N$ goes to infinity the transition region increases which implies that the temperature in the transition region goes to infinity.

# 6 The Self-Induction Approximation for Vortices

The cubic Schrödinger equation is equivalent to the self-induction approximation for vortices [8], which is a widely used equation of motion for a thin vortex filament in classical and superfluid mechanics [1], [7].

We give a very brief introduction to the self-induction approximation here. Consider a vortex filament in three dimensional space. Denote by $\mathbf{x}(s)$ the centerline of the vortex filament, where s is the arclength along the centerline. For inviscid isentropic incompressible fluid it can be shown under some assumptions that the motion of the vortex centerline obeys the following equation [1]

$$\frac{\partial \mathbf{x}(s)}{\partial t} = \kappa(s)\mathbf{b}(s), \tag{14}$$

where $\kappa(s)$ is the curvature, and $\mathbf{b}(s)$ is the binormal to the vortex line, i.e. the vector product $\mathbf{t} \times \mathbf{n}$, where $\mathbf{t}$ is the unit tangent vector, and $\mathbf{n}$ is the unit normal vector to $\mathbf{x}$.

The Frenet-Seret equations of differential geometry are given by

$$\frac{\partial \mathbf{x}}{\partial s} = \mathbf{t}, \qquad \frac{\partial \mathbf{t}}{\partial s} = \kappa\mathbf{n}, \qquad \frac{\partial \mathbf{n}}{\partial s} = \tau\mathbf{b} - \kappa\mathbf{t}, \qquad \frac{\partial \mathbf{b}}{\partial s} = -\tau\mathbf{n}, \tag{15}$$

where $\tau$ is the torsion.

From the equations (14),(15) using the Hasimoto transformation [8]

$$\psi = \kappa exp(i\int_0^s \tau(s)ds), \tag{16}$$

we obtain the cubic Schrödinger equation for $\psi$

$$\frac{1}{i}\frac{\partial \psi}{\partial t} = \frac{\partial^2 \psi}{\partial s^2} + \frac{1}{2}(|\psi|^2 + C)\psi. \tag{17}$$

where C is some function of time only. We can eliminate the function C from the equation above by introducing a change of variables:

$$\tilde{\psi} = \psi \exp(-\frac{i}{2}\int_0^t C(\tau)d\tau), \tag{18}$$

and rewrite equation (17) in the form:

$$\frac{1}{i}\frac{\partial \tilde{\psi}}{\partial t} = \frac{\partial^2 \tilde{\psi}}{\partial s^2} + \frac{1}{2}|\tilde{\psi}|^2\tilde{\psi}. \tag{19}$$

# 7 Changes in the shape of a vortex filament with the constraint $N$ and the temperature

In this section we present the plots of the typical vortex filaments that we obtain from the cubic Schrödinger equation for different values of the constraint $N$ and the temperature. We remarked at the end of Section 5 that in the limit as the constraint $N$ goes to infinity the

temperature at which the transition occurs also goes to infinity. This fact is in agreement with the results of Chorin [5], [4], [6] that the single vortex filament has a phase transition at infinite temperature.

The soliton-like field, which is a typical field configuration for low temperatures and large $N$ (Figure 1) corresponds to an almost straight vortex filament with a sharp kink (see Figure 25)

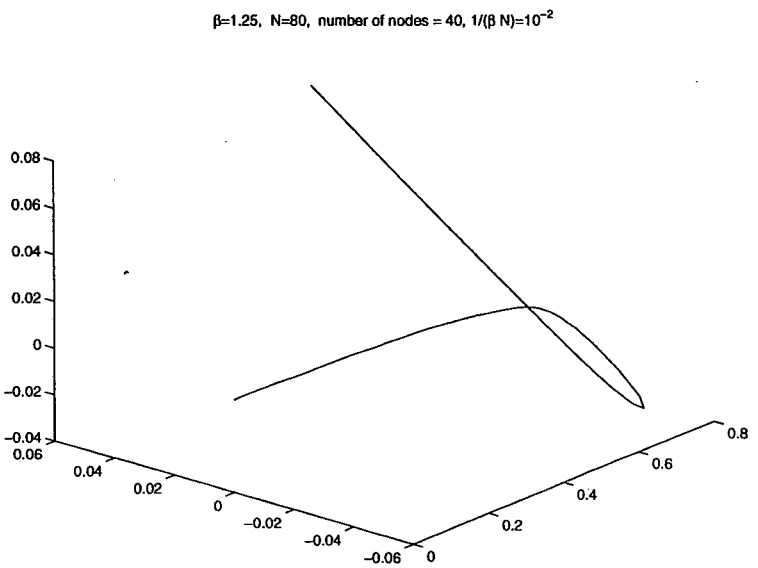


Figure 25: Typical vortex filament for low temperature and large $N$, $\frac{1}{\beta N} = 10^{-2}$

This shape roughly corresponds to the left part of the upper kurtosis function in Figure (4). Keeping the temperature low and decreasing the value of the constraint $N$ gives the left part of the lower kurtosis function in Figure (4); the typical field configuration is close to a constant, and the corresponding filament shape is given in Figure (26). The vortex is smooth and almost circular, which is what one would expect for a constant field, i.e. for constant curvature.

Increasing the temperature destroys the order in the shape of the vortex filament, and the typical vortex becomes more random, as shown in Figure (27); this filament corresponds to the right-hand side of the kurtosis curves in Figure (4).

# 8 Comparison of the Time and Ensemble Averages

Now we present numerical evidence for the equivalence of the ensemble (6), (7) and the microcanonical ensemble; in Figure (28) we show the energy fluctuation of the ensemble (6), (7) around its mean energy, i.e.

$$\frac{< H^2 > - < H >^2}{< H^2 >}, \tag{20}$$

computed at some fixed temperature versus the constraint N.

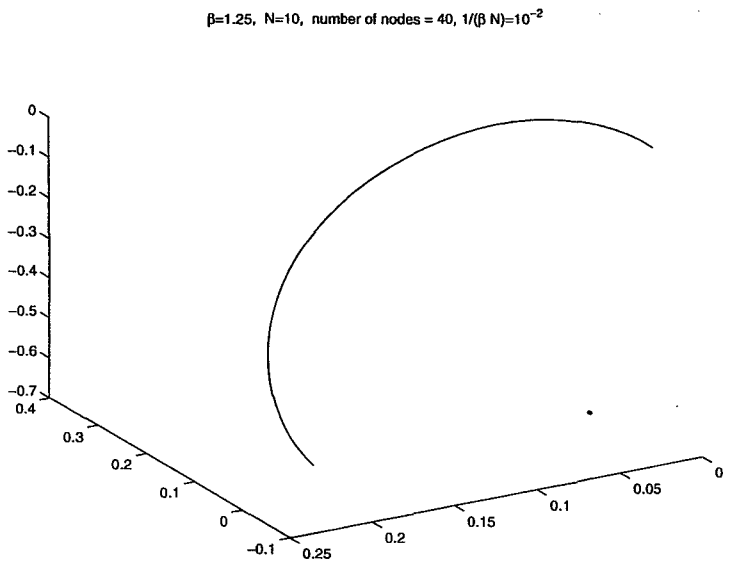


Figure 26: Typical vortex filament for low temperature and small $N$, $\frac{1}{\beta N} = 10^{-2}$

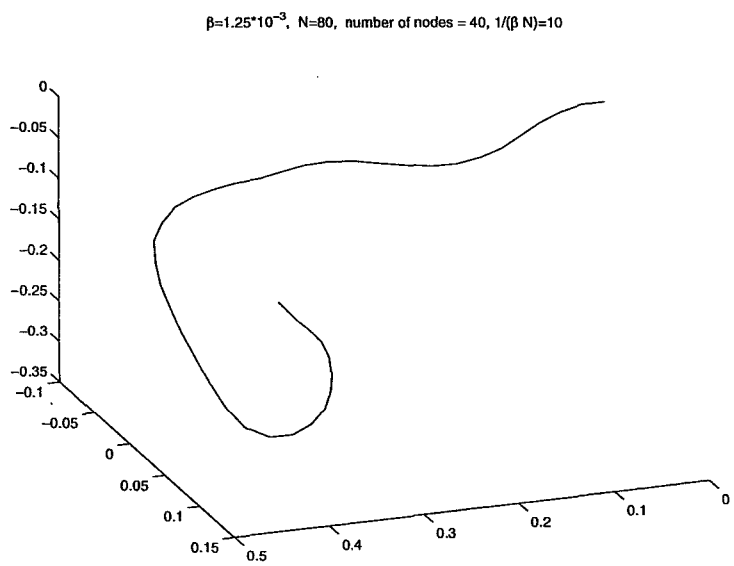


Figure 27: Typical vortex filament for high temperature, $\frac{1}{\beta N} = 10$

We introduce the energy fluctuation (20) into our presentation to estimate the concentration of the measure (6),(7) on the configurations with the mean energy $< H >$. Intuitively it is clear that if the measure (6),(7) is concentrated on the configurations that belong to the energy shell defined by $< H >$, then it is plausible that the averages with respect to (6),(7) and the microcanonical ensemble will be the same.

As one can see from the graph in Figure (28) the energy fluctuation tends to zero as N increases. This suggests that for large values of N the probability density on the space of configurations is concentrated on the energy shell defined by the mean energy $< H >$.

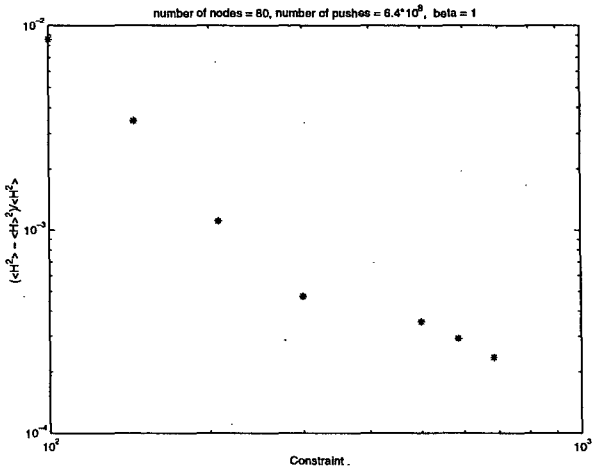


Figure 28: Equivalence of the ensemble (6), (7) and the microcanonical ensemble.

For the dynamical system (3) we choose some initial configuration with the energy equal to the average ensemble energy (6), (7). In Figure (29) we present the calculations of the

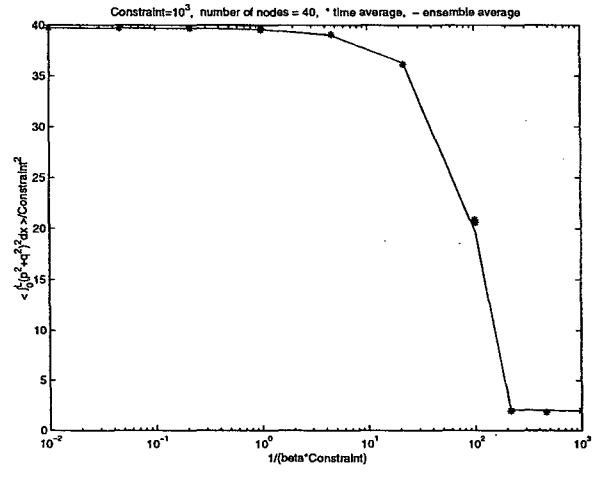


Figure 29: Time average and ensemble average

time average and the ensemble average of the kurtosis $K$ (10). One can see from Figure (29) that there is a remarkable agreement between the time and the ensemble average! In

this computation the number of discretization points was taken to be 40, and the value of the constraint N (13) equal to $10^3$. The same agreement was observed when we increased the number of discretization points to 80 and 150, and changed the value of the constraint. Therefore we conjecture that our discrete dynamical system is ergodic. One remark should be made here about the continuum dynamical system. The cubic Schrödinger equation has an infinite family of conserved quantities (see [16]); the numerical scheme that we use to integrate the cubic Schrödinger equation in time does not have a corresponding infinite family of conserved quantities; although we verify the conservation of the Hamiltonian and the constraint $N$ (13) in the integration in time. Therefore the trajectory in time of the numerical scheme visits a larger subspace than the actual continuum solution, and the ergodicity that we describe here might be due to the particular numerical algorithm.

# 9 Conclusions

We have studied numerically bifurcation and phase transition phenomena in the Gibbs canonical ensemble associated with the cubic Schrödinger equation.

We have shown that the changes in typical function profiles with respect to temperature and constraint observed in [11] are associated with the splitting of a phase space into different components. We discovered that these changes can be observed in a discretization with as few as 2 points.

We point out that the cubic Schrödinger equation is equivalent to the self-induction approximation for vortices [8]. In terms of vortex representation the soliton-like typical structure of functions at low temperatures corresponds to a straight vortex filament with a sharp kink; for high temperatures the straightness of the vortex is destroyed and the shape of the vortex becomes random (Figures 25, 27). We remark that in the limit the temperature at which the transition occurs increases to infinity, which is in agreement with the results of Chorin [5], [4], [6] that the single vortex filament has a phase transition at infinite temperature.

We have investigated numerically the limit of the kurtosis (9) for a fixed number of discretization points as the constraint (7) increases; we demonstrated that eventually the kurtosis converges to a smooth function whose maximum value is determined by the number of discretization points.

We also investigated the limit of kurtosis (9) for a fixed value of the constraint as the number of discretization points increases; we found that the kurtosis converges to a smooth function in this limit as well.

However, if we increase both the constraint (7) and the number of discretization points, then we see a strong numerical indication that for some temperature the first derivative of the kurtosis (9) becomes infinite. We do not know what happens in the infinite limit; however, for large enough values of the constraint and for a large enough number of discretization points there is an indication that there might be a discontinuity in the first derivative of the kurtosis (9), which could indicate a behavior similar to a phase transition in classical statistical mechanics.

We also have shown the equivalence of the Gibbs canonical ensemble associated with the cubic Schrödinger equation (6),(7) and the microcanonical ensemble (Figure (29)).

We have studied the ergodicity of the system (3) (6),(7), and presented results that show the equivalence of time and ensemble averages (Figure 29). We remarked that the numerical method used for integrating the cubic Schrödinger equation in time has two constants of motion: the Hamiltonian (4) and the constraint (7). On the other hand the cubic Schrödinger equation has an infinite number of conserved quantities [16], so the relation of this numerical result to the discretized equations of motion for the continuum cubic Schrödinger equation is not straightforward. However, it is still an interesting fact that in the discrete version of the cubic Schrödinger equation there is an equivalence of the time and ensemble averages.

# 10 Acknowledgements

The author thanks Alexandre Chorin for numerous helpful discussions and suggestions.

# References

[1] G.K.Batchelor *An Introduction to Fluid Dynamics*, Cambridge University Press, London, 1967.

[2] K.Binder D.W.Heermann *Monte Carlo Simulation in Statistical Physics* Springer-Verlag, New York Berlin Heidelberg 1992

[3] T.Buttke *A Numerical Study of Superfluid Turbulence in the Self-Induction Approximation*, Journal of Computational Physics 76, 301-326, 1988.

[4] A.J.Chorin *Vorticity and Turbulence* Springer-Verlag, New York, 1994

[5] A.J.Chorin *Equilibrium statistics of a vortex filament with applications*, Communications in Mathematical Physics, 141(3), pp.619-631, 1991.

[6] A.J.Chorin, J.Akao *Vortex equilibria in turbulence theory and quantum analogues*, Physica D 51 (1991), pp. 403-414.

[7] R.P.Feynman *Application of quantum mechanics to liquid helium*, Progress in Low Temperature Physics, 1955.

[8] H.Hasimoto *A Soliton On a Vortex Filament*, J.Fluid Mech., 51 (1972), pp.477-485

[9] K.Huang *Statistical Mechanics*, John Wiley & Sons, New York, 1987.

[10] R.Klein, A.Majda *Self-stretching of perturbed vortex filaments 2. Structure of solutions*, Physica D 53, 1991, pp. 267-294

[11] J.L.Lebowitz, H.A.Rose, E.R.Speer *Statistical Mechanics of the Nonlinear Schrödinger Equation*, Journal of Statistical Physics, Vol. 50, Nos 3/4, 1988

[12] H.P.McKean *Statistical Mechanics of Nonlinear Wave Equations (4): Cubic Schrödinger*, Communications in Mathematical Physics, vol.168 (1995), p. 479-491

[13] H.P.McKean, K.L.Vaninsky *Statistical Mechanics of Nonlinear Wave Equations*, Preprint, CIMS, 1993.

[14] H.P.McKean, K.L.Vaninsky *Brownian motion with restoring drift: the petit and micro-canonical ensembles*, Communications in Mathematical Physics, vol.160, (no.3), 1994. p.615-30

[15] N.Metropolis, A.W.Rosenbluth, M.N.Rosenbluth, A.H.Teller, E.Teller J.Chem.Phys 21, 1087, 1953

[16] A.C.Newell *Solitons in Mathematics and Physics*, SIAM, Philadelphia, 1985.

[17] K.W.Schwarz *Turbulence in superfluid helium: Steady homogeneous counterflow*, Physical Reviews B, 18, pp.245-262, 1978.

ERNEST ORLANDO LAWRENCE BERKELEY NATIONAL LABORATORY
ONE CYCLOTRON ROAD | BERKELEY, CALIFORNIA 94720

Prepared for the U.S. Department of Energy under Contract No. DE-AC03-76SF00098